

Full Length Article

Multilayer activated biochar/UiO-66-NH₂ film as intelligent sensing platform for ultra-sensitive electrochemical detection of Pb²⁺ and Hg²⁺

Jin Zou^{a,b}, Wenbin Qian^a, Yihui Li^a, Qi Yu^a, Yongfang Yu^a, Shangxing Chen^{a,*}, Fengli Qu^{b,*}, Yansha Gao^a, Limin Lu^{a,*}

^a East China Woody Fragrance and Flavor Engineering Research Center of NF&GA, Key Laboratory of Chemical Utilization of Plant Resources of Nanchang, College of Forestry, School of Software, Jiangxi Agricultural University, Nanchang 330045, PR China

^b College of Chemistry and Chemical Engineering, Qufu Normal University, Qufu Shandong 273165, PR China



ARTICLE INFO

Keywords:

Layer-by-Layer assembly
Electrodeposition
Artificial Neural Network
Biochar
Metal Organic Framework

ABSTRACT

In this work, a novel electrochemical sensor based on multilayer activated biochar (AC)/Zr-metal-organic frameworks ([AC/UiO-66-NH₂]), combining with artificial neural network (ANN) integrated system is proposed for simultaneous determination of Pb²⁺ and Hg²⁺ in water samples. The layer-by-layer (LbL) deposition technique is adopted to obtain multi-layer film of [AC/UiO-66-NH₂] with adjustable surface structure and controllable thickness. UiO-66-NH₂ with porous structures and high specific surface area is profitable to the adsorption and preconcentration of Pb²⁺ and Hg²⁺, meanwhile, the use of AC that is activated by KOH can enlarge the active surface area of the electrode, increase the conductivity and load of UiO-66-NH₂. Besides, the layered structure of composite film provides more mass transfer channels, increases ions and electronic diffusion coefficient and creates more additional active sites. Attributing to these impressive features, the detection signals of Pb²⁺ and Hg²⁺ are greatly amplified on the [AC/UiO-66-NH₂]₂ modified electrode. Both the Pb²⁺ and Hg²⁺ can be detected with the detection limit down to 1.0 ng·L⁻¹. In addition, the integration of the prepared sensor and the ANN system is capable of the prediction of Pb²⁺ and Hg²⁺ concentrations in water samples with the recovery ranging from 95.93% to 101.4%. Results from ANN model present high correlation (0.99991 and 0.99993 for Pb²⁺ and Hg²⁺, respectively) with those from the experiments, validating the promising application for sensing analysis.

1. Introduction

With the advancement in industrialization and technology, heavy metal pollution as the most common environmental problem is increasingly prominent [1]. A majority of heavy metal ions (HMIs) are highly toxic and can easily enter the human body to be bioaccumulated along the food chain, posing a grave threat to human health [2–4]. As a result, developing effective, ecofriendly, and economic methods for the trace detection of heavy metal ions is imperative. Electrochemical methods have attracted tremendous attention for the detection of HMIs ascribing to their advantages of cost-effectiveness, simple operation, and outdoor detection. More importantly, electrochemical sensors can be miniaturized and intelligent [5]. The electrode materials play a vital role in raising the catalytic activity of the electrochemical sensor, where ideal candidates should have the basic features of large specific surface area, high adsorption capacities for analytes, good electrical

conductivity and stability [6,7].

Metal-organic frameworks (MOFs), building from metal ions or clusters and multifunctional organic ligands, belong to a promising class of porous crystalline inorganic-organic hybrid materials [8]. Owing to their well-regulable physiochemical properties and large specific surface area, MOFs have attracted increasing attention as electrode materials/modifiers. MOFs with huge cavity and porous thin wall, MOFs can allow electrolyte and ions enter easily, providing more electrochemical active sites. Besides, the abundant heteroatoms in ligands can interact with electron-deficient HMIs [9]. Based on these fascinating properties, several MOFs, such as ZIF-67 [10], JUC-62 [11], and MIL-53(Al) [12], have been applied as recognition elements in electrochemical sensor. Nevertheless, the intrinsic shortcomings of MOFs, such as poor electrical conductivity and low stability limit their wide applications. In this case, coupling MOFs with conductive nanomaterials to construct a nano-structure hybrid, has been proved to be one of available approaches to

* Corresponding authors.

E-mail addresses: csxing@126.com (S. Chen), fengliqun@hotmail.com (F. Qu), lulimin816@hotmail.com (L. Lu).

<https://doi.org/10.1016/j.apsusc.2021.151006>

Received 16 July 2021; Received in revised form 11 August 2021; Accepted 16 August 2021

Available online 27 August 2021

0169-4332/© 2021 Elsevier B.V. All rights reserved.

improve the electron transfer ability and stability of the MOFs [7,13].

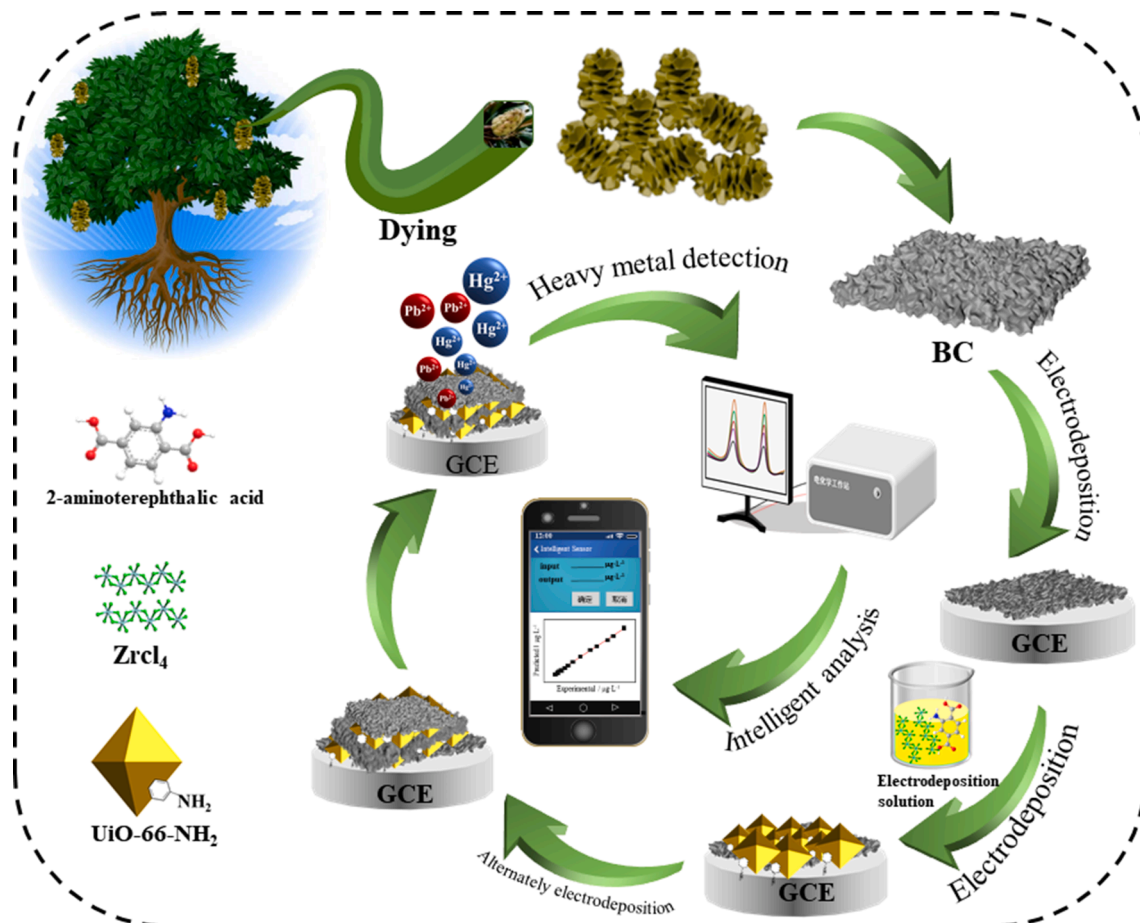
In recent years, carbon materials, especially derived from biomass, have received great attention as one kinds of the most promising electrode conductive materials. Compared to graphene [14] and CNTs [15], biochar exhibits some other distinct advantages, e.g i) The sources of biochar are widespread and their preparation is easy. ii) Rich functional groups, such as carboxyl, hydroxyl, and phenolic groups on biochar surface can effectively enrich the analytes through electrostatic attraction and ion exchange action. iii) The surface structure and surface activity of biochar can be easily regulated by chemical reagents, such as nitric acid [16], sodium hydroxide [17]. All of these advantages of biochar inspire us to combine the activated biochar (AC or AB) with MOFs to fabricate an effective sensing platform for determination of heavy metal ions.

It is well known that the performance of nanomaterials-based electrochemical sensors strongly correlates to the physical structure of the sensing interface. Generally, the fabrication of MOF-based electrodes is mainly prepared by drop-coating method. However, the directly casting method for practical application will result in a weak adhesion to substrate electrodes. Additionally, the formed inhomogeneous film will lead to poor reproducibility of electrodes. In comparison, layer-by-layer (LbL) technique is an utility and inexpensive way to modify solid substrates with functional films [18]. By the alternating LbL deposition process, homogeneous MOFs-based film with well-defined thickness can be obtained on the modified electrode. For example, Lu et al. [19] have fabricated a sensitive MWCNTs-COOH/UiO-66-NH₂/ MWCNTs-COOH electrochemical sensing interface by LbL electrodeposition method. Nevertheless, in this system, the deposition of MOFs on the electrode still requires multiple steps, including hydrothermal and electrodeposition process. In fact, MOFs can be formed by direct deposition in

mother liquor system at a certain voltage [20]. Accordingly, it can be expected that the LbL assembly of [AC/UiO-66-NH₂] film can be facilely synthesized in UiO-66-NH₂ mother solution and AC solution.

For practical sensors, besides good sensitivity, effective data analysis is also an important indicator. The data analysis in traditional electrochemical sensing system is mainly relied on different traditional regression methods. These analysis methods can model well in linear systems; however, they are powerless when encountering the problems of overlapping signals or difficult nonlinear quantization [21]. Artificial neural network (ANN), one of artificial intelligence (AI) methods, can well estimate or approximate functions from sample data, which is deemed as an efficient computing model in sensor applications. They can intelligently mine the rules in given data sets and establish the corresponding analysis model. They only need input and output variables, while the research of the relationships between process parameters is not necessary [22]. In comparison with traditional electrochemical large-workstation, the system has higher accuracy and reliability in linear/nonlinear correlation, can adapt to real-time operation and calculate the results within a short time [23]. In the past few years, the combination of electrochemical sensing platform with ANN modeling has been well employed in the analysis of pesticides [24], plant growth regulators [25] and phenolic compounds [22].

Based on the above considerations, laminated composite film of [AC/UiO-66-NH₂] coupled with ANN algorithm has been proposed for the simultaneous detection of Pb²⁺ and Hg²⁺ with ultra-trace level in water (Scheme 1A). AC and UiO-66-NH₂ were alternately grown on the glassy carbon electrode to form LbL multilayer [AC/UiO-66-NH₂] film. The strong Zr-O bond endows Zr-based MOFs excellent chemical/hydrothermal stability, versatility and the ability of adsorbing Pb²⁺ and Hg²⁺. The active group of -NH₂ can also interact with electron-deficient Pb²⁺



Scheme 1A. Schematic illustration of the preparation process of [AC/UiO-66-NH₂]₂ electrode.

and Hg^{2+} . Moreover, AC with excellent properties of hierarchical porosity, good conductivity, and abundant oxygen-containing functional groups can further improve the electron transfer rate and enrichment of Pb^{2+} and Hg^{2+} on electrode surface. Consequently, the current strategy displays superior sensing performance with high sensitivity, satisfactory stability and good selectivity. Combining with ANN algorithm, real-time applicability of the proposed sensor can be employed to quantify Pb^{2+} and Hg^{2+} concentration in river water and paddy water.

2. Experimental section

2.1. Reagents and chemicals

N, N-dimethylformamide (DMF, 99.5%), zirconium tetrachloride (ZrCl_4 , 98%), 2-amino-terephthalic acid ($\text{NH}_2\text{-H}_2\text{BDC}$, 98%), lead nitrate ($\text{Pb}(\text{NO}_3)_2$, $\geq 99\%$), and mercury nitrate ($\text{Hg}(\text{NO}_3)_2$, $\geq 99\%$) were purchased from Sinopharm Chemical Reagents Co., Ltd (Shanghai, China). 0.1 mol/L acetate buffer solution (pH 4.5) was prepared by mixing the appropriate amounts of sodium acetate and acetic acid. All reagents are used as received without further purification.

2.2. Apparatus

AC samples were prepared in a tubular furnace (OTF-1200X, Hefei Kejing materials technology Co., Ltd., Hefei, China). All electrochemical experiments were carried out on a CHI 660E electrochemical workstation (CHI Instrument Co., Ltd., Shanghai, China) with a three-electrode system, which consisting of a working electrode (GCE with diameter of 3 mm), a counter electrode (platinum wire), and a reference electrode (saturated calomel electrode (SCE)). The device has a length of 37 cm, a width of 23 cm and a height of 12 cm. Various techniques such as X-ray diffraction (XRD/D8 Advance, Germany), X-ray photoelectron spectroscopy (XPS/ThermoFischer Escalab 250Xi, USA), Fourier Transform Infrared Spectrometer (FT-IR/Nicolet-6700, USA), Brunauer-Emmett-Teller (BET/NOVA 4200e, USA) and scanning electron microscopy (SEM/Zeiss Gemini 300, Germany) were studied. In the model design, the feed-forward back propagation artificial neural network is realized by Python 3.6.1.

2.3. Preparation of AC

Magnolia grandiflora fruit derived AC was produced by slowly pyrolyzing the feed stock under a nitrogen protection. Firstly, the surface of Magnolia grandiflora fruit was briefly washed with water to remove impurities. The dried Magnolia grandiflora fruit was grinded into powder and activated with KOH solution. The resulted product was placed in a tubular furnace and heated for 2 h in N_2 atmosphere. The heating rate and the final temperature were set to $5^\circ\text{C}/\text{min}$ and 800°C , respectively. Finally, the obtained AC material was ground into powder and a certain amount of AC was dispersed in water to prepare AC solution (0.3 mg/mL) for subsequent experiments

2.4. Preparation of working electrode

Before modification, GCE surface was polished with $0.3\ \mu\text{m}$ alumina slurry, and then rinsed by deionized water and ethanol. The pretreated electrode was immersed in AC solution and deposited at 1.7 V for 300 s to prepare AC/GCE. The AC/GCE was gently washed with ultrapure water and placed in DMF solution containing 1 mM ZrCl_4 and 1 mM H_2BDC . After electrodeposition for 200 s at $-1.8\ \text{V}$ [26], UiO-66-NH₂ layer was formed on AC/GCE. The above steps were repeated several times to obtain $[\text{AC}/\text{UiO-66-NH}_2]_n$ multilayer film GCE. The fabrication process and detection mechanism of electrochemical sensor based on LbL self-assembly technology are shown in Scheme 1A.

2.5. ANN model

Artificial neural networks inspired by biological neural networks in the brain are an interesting mathematical modeling tool, which have been proved to be able to solve nonlinear problems and successfully applied for modeling complex relationships between dependent variables and independent variables [27]. The structure diagram of feed-forward back-propagation neural network is presented in Scheme 1B. Structurally, ANN model is a multilayer perceptron (MLP), consisting of input layer, hidden layer and output layer. Gradient descent-based algorithm is used in the ANN model, which minimizes the mean square error (MSE) between the ANN's output and the desired output for all the input patterns [28]. The neurons between each layer are connected by different links of diverse weights and the output is calculated by a transfer function. Therefore, the structure of the ANN model is depended on the number of layers, respective number of neurons in each layer and the properties of the transfer function. In this study, the ANN modeling with $2 \times 20 \times 1$ architecture was adopted. The neurons in the input layer receive the response of the electrochemical sensor and contain 2 input nodes; the hidden layer neurons simulate the biological neural network to transmit information and are determined as 20 nodes by trial-error method; the neurons in the output layer represent the analyte concentration have 1 output nodes; The activation function is relu, and the maximum number of iterations is set to 5000.

2.6. Evaluation of ANN performance

The determination coefficients of calibration set (R_c^2) and cross validation set (R_{cv}^2), root means square error of calibration set (RMSE_c) and cross validation set (RMSE_{cv}), mean absolute error (MAE) were adopted to appraise the performance of ANN model. The closer R^2 is to 1, the fitting performance of the model is better. While, the smaller the RMSE value, the prediction model is the better.

$$R^2 = \frac{\sum_{i=1}^n (f_{EXP,i} - \bar{f}_{EXP})(f_{ANN,i} - \bar{f}_{ANN})}{\sqrt{\sum_{i=1}^n ((f_{EXP,i} - \bar{f}_{EXP,i})^2 (f_{ANN,i} - \bar{f}_{ANN,i})^2)}} \quad (1)$$

$$\text{RMSE} = \sqrt{\frac{\sum_{i=1}^n (f_{EXP,i} - f_{ANN,i})^2}{n}} \quad (2)$$

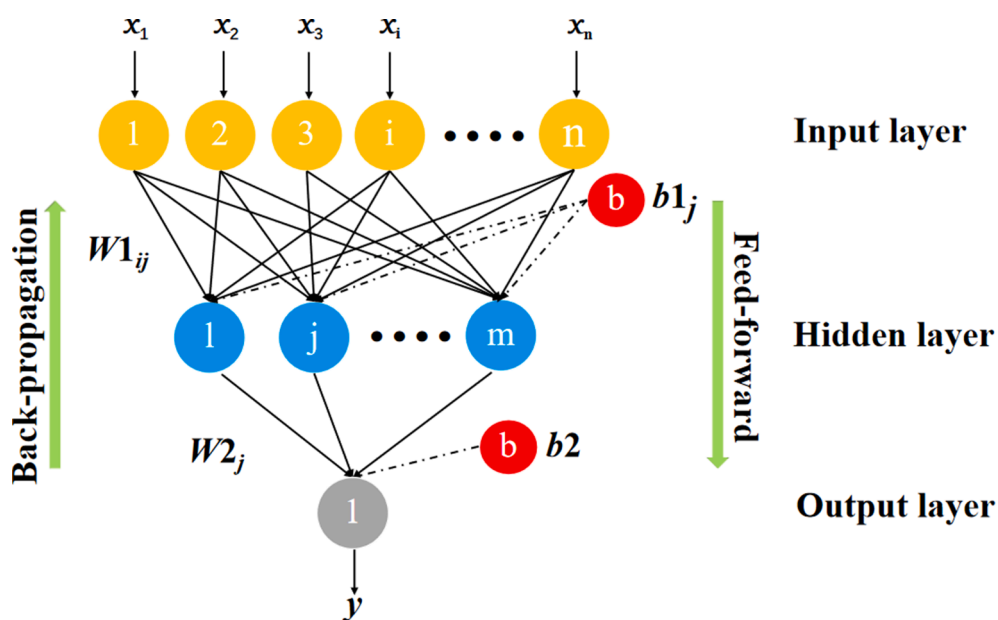
$$\text{MAE} = \frac{1}{n} \sum_{i=1}^n |f_{EXP,i} - f_{ANN,i}| \quad (3)$$

Where, $f_{EXP,i}$ and $f_{ANN,i}$ are the experimental value and ANN predicted value of sample, \bar{f}_{EXP} and \bar{f}_{ANN} are the average value of experimental and ANN predicted value, n is the number of the sample [29].

3. Results and discussion

3.1. Morphology and structure characterization

The morphologies of AC, UiO-66-NH₂ and $[\text{AC}/\text{UiO-66-NH}_2]_2$ composites were studied by SEM. As shown in Fig. 1A, UiO-66-NH₂ shows a stereoscopic structure with small octahedral cubic intergrown crystals, and its size is about 50 ~ 200 nm. Fig. 1B is the SEM image of AC activated by KOH. It can be seen that the AC shows rough and porous structure, owing to the fact that KOH activation can generate nanopores and defects by removing atoms from the carbon skeleton [30]. Such a porous texture is beneficial to the improvement of mass transfer performance. As for $[\text{AC}/\text{UiO-66-NH}_2]_2$ (Fig. 1C), a large number of UiO-66-NH₂ nanoparticles are homogeneously attached on the surface of AC, which provides more active sites for enrichment of heavy metal ions. Notably, from the section SEM image of $[\text{AC}/\text{UiO-66-NH}_2]_2$ (Fig. 1D), the multilayer structure can be clearly observed, which indicates that



Scheme 1B. Schematic architecture of ANN according to the considered input and output parameters and feed-forward back-propagation algorithm. (x : input value; W : the synaptic weight; b : bias vectors; y : output value).

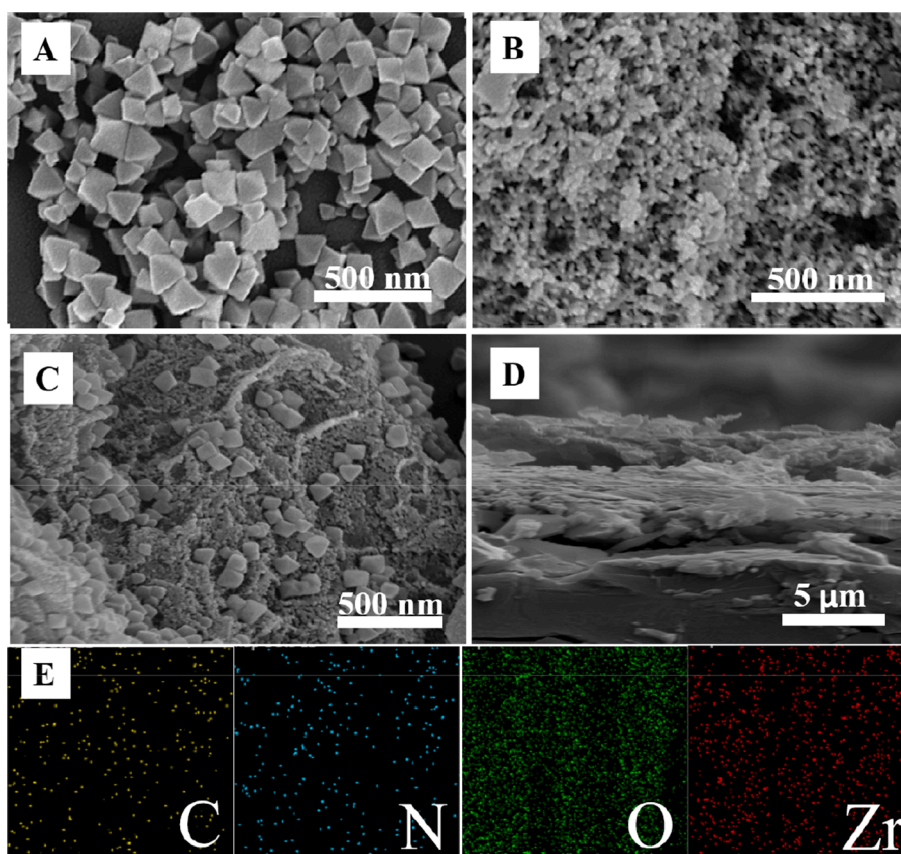


Fig. 1. SEM images of (A) UiO-66-NH₂, (B) AC, (C) [AC/UiO-66-NH₂]₂ film and (D) cross-sectional view of [AC/UiO-66-NH₂]₂. (E) EDX mapping of C, N, O and Zr elements.

LbL assembly is an effective method to fabricate multilayer structures. From the mapping result (Fig. 1E), elements of C, N, O and Zr are evenly distributed in the [AC/UiO-66-NH₂]₂ composite.

The crystallographic structures of AC, UiO-66-NH₂ and [AC/UiO-66-NH₂]₂ were characterized by XRD. As shown in Fig. 2A, the XRD profile

of pristine UiO-66-NH₂ displays major diffractions at 12.9°, 14.7°, 17.9°, 19.7°, 21.4°, 23.2°, 28.7°, 31.1°, 33.5°, 35.9°, 36.9°, 40.1°, 42.9° and 50.5°, which are in good accordance with previous reports [19], corroborating the successful preparation of the UiO-66-NH₂ crystalline framework. For AC, it displays two diffraction peaks at about 21° and

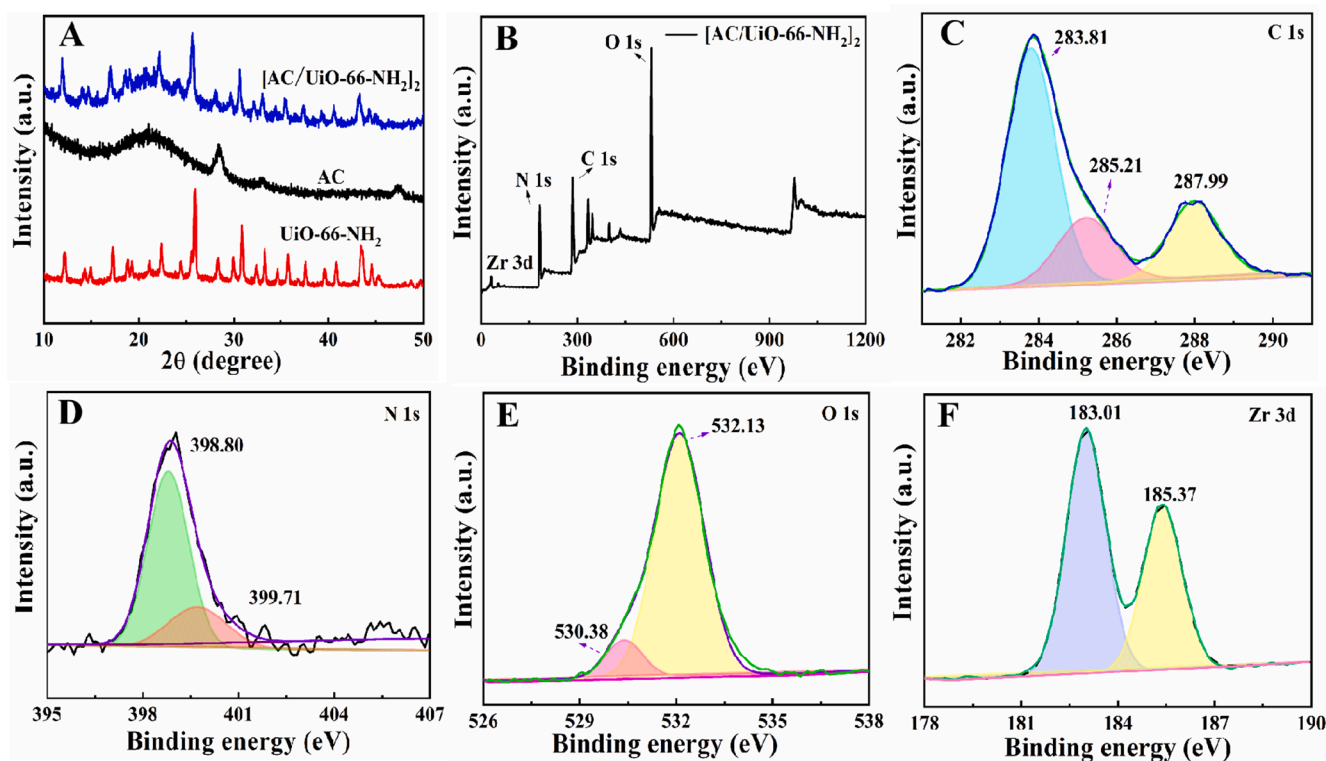


Fig. 2. (A) XRD pattern and (B) Full-scan XPS spectra and (C) C 1 s, (D) N 1 s, (E) O 1s, and (F) Zr 3d XPS spectra of [AC/Uio-66-NH₂]₂ multilayer film.

27.3°, which is consistent with the (002) and (111) diffraction planes of graphite lattice, respectively. In addition, a shape peak at about 48° is corresponded to the (100) planes of graphitic carbon, indicating the formation of graphite structure to a certain extent [31]. As for [AC/Uio-66-NH₂]₂, its spectrum is matched well with that of pure Uio-66-NH₂ and AC, which further confirms the successful development of [AC/Uio-66-NH₂]₂.

XPS was performed to determine the surface chemical composition of [AC/Uio-66-NH₂]₂.

As exhibited in Fig. 2B, four main elements of C, N, O and Zr are observed from the full survey of [AC/Uio-66-NH₂]₂. For further analysis of the element states, the fine spectrum of each element was studied. C 1 s spectrum in Fig. 2C is decomposed into three peaks located at 283.81 eV (C-C & C-H), 285.21 eV (C-N) and 287.99 eV (C = O), respectively [32]. The deconvolution N 1 s spectrum consists of two contributions at 398.81 eV and 399.71 eV, corresponding to amino (-NH₂) and protonated amino (-NH₃⁺), respectively (Fig. 2D) [19]. In Fig. 2E, the O 1 s signals appear at 530.38 eV and 531.54 eV, which can be assigned to Zr-O and C-O. In addition, two distinguishable peaks positioned at 183.01 eV and 185.37 eV in the Zr 3d fine spectrum belong to Zr 3d^{5/2} and Zr 3d^{3/2}, respectively (Fig. 2F) [33].

FTIR spectroscopy was employed to confirm the surface functional groups of Uio-66-NH₂, AC, and [AC/Uio-66-NH₂]₂ (Fig. 3). In case of AC, the characteristic absorption peak at 1573 cm⁻¹ can be assigned to the stretching vibration of aromatic C = C bonds. The weak peaks at 1377 and 1214 cm⁻¹ are accounted for the stretching vibration of the epoxy bond, whereas the peak at 1035 cm⁻¹ is attributed to the stretching vibration of alkoxy. The bands at 1710 and 3276 cm⁻¹ are ascribed to the stretching of C = O and -OH, respectively [32]. These results affirm the presence of functional groups on the AC, such as hydroxyl, carboxylate, and phenolic hydroxyl. In terms of pure Uio-66-NH₂, the peak around 3361 cm⁻¹ is assigned to the stretching mode of primary amines. The vibration peaks at 1565 cm⁻¹ and 1633 cm⁻¹ are caused by the coordination reaction between the carboxyl group in NH₂-BDC and the Zr⁴⁺. The peaks at 1497, 1394 and 1257 cm⁻¹ belong to the

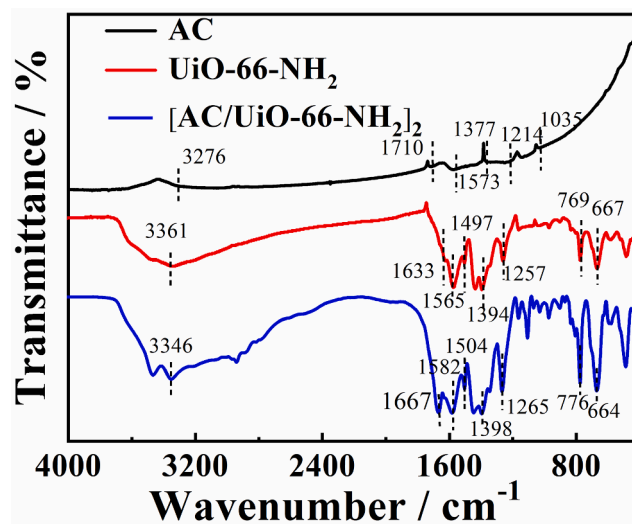


Fig. 3. FT-IR spectra of AC, Uio-66-NH₂ and [AC/Uio-66-NH₂]₂ films.

N-H, C-C and C-N tensile vibration peaks, respectively. The absorption peaks at 667 and 769 cm⁻¹ are assigned to Zr-O bands [19,33]. In the FT-IR spectra of [AC/Uio-66-NH₂]₂ composite, the characteristic peaks are basically the same with that of Uio-66-NH₂. Owing to the high intensity of Uio-66-NH₂, the characteristic diffraction peaks of AC in [AC/Uio-66-NH₂]₂ are not obvious.

Fig. 4A presents the nitrogen adsorption/desorption isotherms of the AC, Uio-66-NH₂ and [AC/Uio-66-NH₂]₂ at 77 k. All samples exhibit reversible sorption with a typical type I curve, indicating typical characteristic of microporous structure [34]. Meanwhile, the [AC/Uio-66-NH₂]₂ composite shows an obvious hysteresis loop in the ranges of 0.4–1.0P/P₀, which is in concert with the results of pore size distribution (Fig. 4B), demonstrating the presence of mesopores. Porous structural

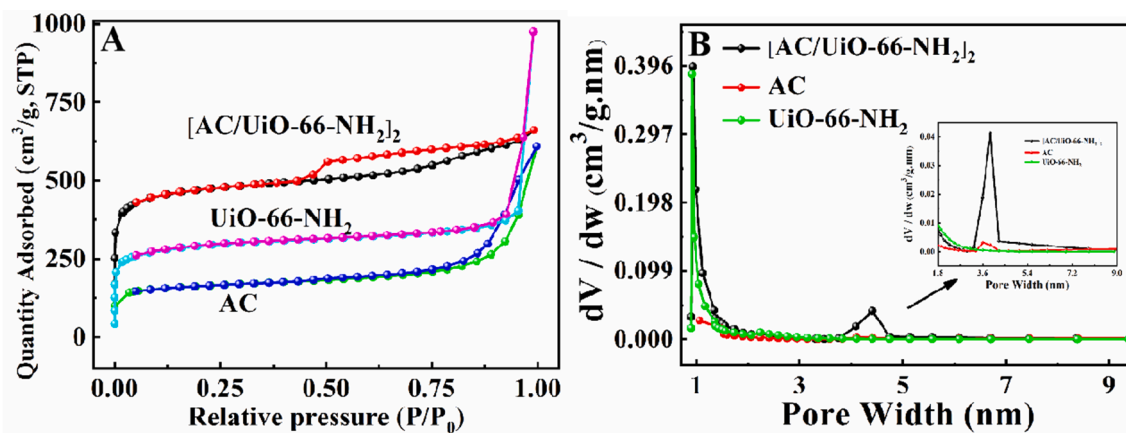


Fig. 4. (A) Nitrogen adsorption/desorption isotherms and (B) pore size distributions of AC, UiO-66-NH₂ and [AC/UiO-66-NH₂]₂.

data of the materials are presented in Table 1. Compared with UiO-66-NH₂ and AC, [AC/UiO-66-NH₂]₂ displays an enlarged surface area (1477.42 m²·g⁻¹) and total pore volume (0.9604 cm³·g⁻¹), suggesting that the introduction of AC improves the pore structure and expands the interlaminar space of the composites. Meanwhile, new holes are created at the two-phase interfaces.

3.2. Electrochemical characterization of different modified electrodes

Electrochemical impedance spectroscopy (EIS) is a powerful method for the study of the electron transfer behavior of different electrodes. Fig. 5A exhibits the Nyquist plots of various electrodes, which reflects the electron-transfer resistance (R_{et}) corresponding to semicircles [35]. Furthermore, the impedance data can be obtained from Randles circuit model (insert part in Fig. 5A), made of Warburg impedance (Z_w), electrode surface resistance (R_s), double-layer capacitance (Cdl) and R_{et} . Accordingly, the R_{et} value is found to be 877.6 Ω for bare GCE. While, AC/GCE displays the almost disappeared semicircle with a R_{et} value of 42.13 Ω , indicating the good transfer efficiency and conductivity of AC. The deposition of UiO-66-NH₂ on AC/GCE causes an enlarged R_{et} value of 1099.79 Ω for the resulted [AC/UiO-66-NH₂]₂/GCE, which is ascribing to the low electrical conductivity of MOF.

To study electrochemical behaviors of [AC/UiO-66-NH₂]₂/GCE for simultaneous detection of various heavy metal ions, the DPASV responses of 100 $\mu\text{g}\cdot\text{L}^{-1}$ Pb²⁺ and 100 $\mu\text{g}\cdot\text{L}^{-1}$ Hg²⁺ were recorded in 0.1 M acetate buffer solution (pH = 4.5). The electrochemical analysis includes three steps: (i) accumulation process; (ii) electrochemical reductive process; (iii) electrochemical oxidative process [36]:

- I. adsorption process: ([AC/UiO-66-NH₂]₂/GCE) surface + (Pb²⁺, Hg²⁺) solution \rightarrow (Pb²⁺, Hg²⁺...[AC/UiO-66-NH₂]₂/GCE) surface
- II. electrochemical reductive process: (Pb²⁺, Hg²⁺...[AC/UiO-66-NH₂]₂/GCE) surface + 2e⁻ \rightarrow (Pb⁰, Hg⁰...[AC/UiO-66-NH₂]₂/GCE) surface
- III. electrochemical oxidative process: (Pb⁰, Hg⁰...[AC/UiO-66-NH₂]₂/GCE) surface \rightarrow (Pb²⁺, Hg²⁺) solution + ([AC/UiO-66-NH₂]₂/GCE) surface + 2e⁻

Table 1

Textural properties of AC, UiO-66-NH₂ and [AC/UiO-66-NH₂]₂.

Sample name	Specific surface area (m ² g ⁻¹)	Micro-pore volume (cm ³ g ⁻¹)	Total pore volume (cm ³ g ⁻¹)
AC	519.56	0.1695	0.5712
UiO-66-NH ₂	918.46	0.2972	0.5756
[AC/UiO-66-NH ₂] ₂	1477.42	0.5476	0.9604

The DPASV curves obtained from bare GCE, AC/GCE, UiO-66-NH₂/GCE, and AC/UiO-66-NH₂/GCE were also presented for comparison. As shown, two weak stripping peaks for Pb²⁺ and Hg²⁺ are observed at bare GCE. Nevertheless, the stripping peak currents significant increase at AC/GCE, which is due to the excellent electric conductivity and porous structure of AC. Besides, the negative charge of functional groups on AC furnishes strong affinity for metal cations [37]. UiO-66-NH₂/GCE shows stripping peak currents three times higher than that at bare GCE. The reinforced peak currents can be ascribing to the porous structure of the NH₂-UiO-66, which promotes the diffusion and preconcentration of metal ions. The combination of AC and UiO-66-NH₂ leads to further advancement in the electrocatalytic activity of AC/UiO-66-NH₂/GCE and [AC/UiO-66-NH₂]₂/GCE toward Pb²⁺ and Hg²⁺. Distinctly, [AC/UiO-66-NH₂]₂/GCE presents higher stripping peak currents than AC/UiO-66-NH₂/GCE. This phenomenon is because that Pb²⁺ and Hg²⁺ can be adsorbed into the pores of the layered structure. In addition, the prepared AC/UiO-66-NH₂ contains abundant nitrogen and oxygen active sites uniformly distributed on the surface or inside the materials. Pb²⁺ and Hg²⁺ can easily coordinate with ligands to form composite materials, which is beneficial to the highly sensitive detection. Therefore, the [AC/UiO-66-NH₂]₂/GCE presents an electrochemical platform with advantageous and high performance for detection of Pb²⁺ and Hg²⁺.

The effective surface areas of [AC/UiO-66-NH₂]₂/GCE was determined by cyclic voltammetry at different scan rates in 5 mM [Fe(CN)₆]^{3-/4-} containing 0.1 M KCl (Fig. 6). According to the Randles-Sevcik principle [38,39], the electrochemical surface area can be calculated by the following equation:

$$I_p = 2.69 \times 10^5 AD^{1/2} n^{3/2} \nu^{1/2} C$$

Where, I_p is the cathodic peak current. A stand for the effective area of the electrode. D (7.6×10^{-6} cm²·s⁻¹) and n ($n = 1$) refer to the diffusion coefficient and electron transfer number of [Fe(CN)₆]^{3-/4-}, respectively. C is the concentration of the probe molecule (5 mM [Fe(CN)₆]^{3-/4-}). ν is the scan rate. From the slope of the $I_p - \nu^{1/2}$ relationship, the effective surface area of the [AC/UiO-66-NH₂]₂/GCE is calculated to be 1.060 cm². The lamellar structure and the abundant micropores of the [AC/UiO-66-NH₂]₂ are the main reasons for the enhanced electrolyte-electrode effective contact area.

3.3. Optimization of the experimental conditions

To acquire the maximum sensitivity for simultaneous detection of Pb²⁺ and Hg²⁺, some critical experimental conditions including pH of the supporting electrolyte, deposition potential and deposition time were studied in the electrolyte containing 100 $\mu\text{g}\cdot\text{L}^{-1}$ Pb²⁺ and Hg²⁺.

The DPASV responses towards 100 $\mu\text{g}\cdot\text{L}^{-1}$ Pb²⁺ and 100 $\mu\text{g}\cdot\text{L}^{-1}$ Hg²⁺

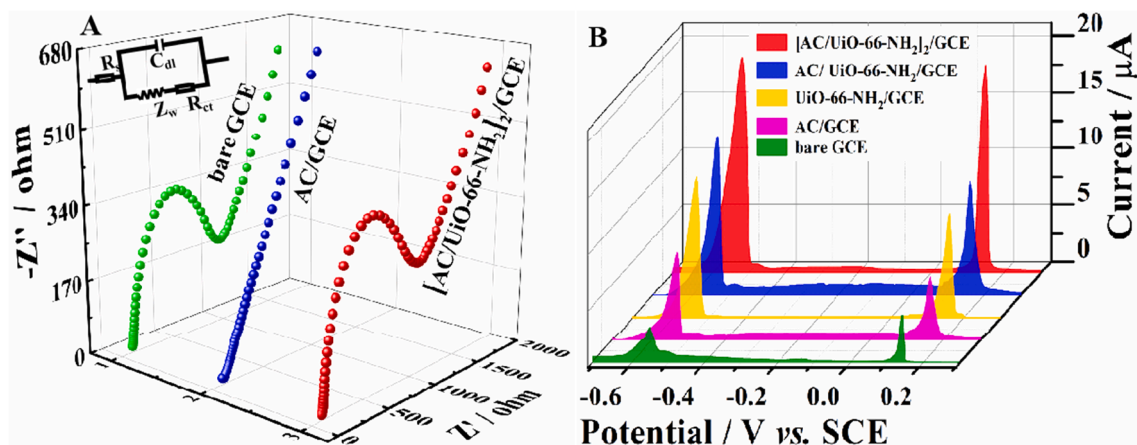


Fig. 5. (A) Electrochemical Impedance Spectroscopy of bare GCE, AC/GCE and [AC/UiO-66-NH₂]₂/GCE; (B) DPASV of 100 µg·L⁻¹ Pb²⁺ and Hg²⁺ at the bare GCE, AC/GCE, UiO-66-NH₂/GCE, AC/UiO-66-NH₂/GCE and [AC/UiO-66-NH₂]₂/GCE in 0.1 mol·L⁻¹ acetate buffer solution (pH = 4.5).

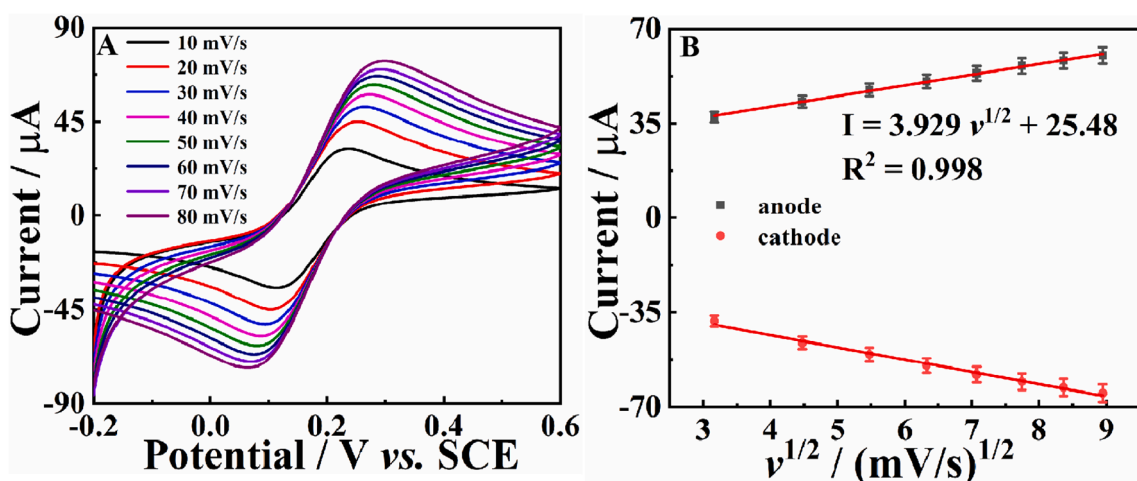


Fig. 6. (A) CV curves of the [AC/UiO-66-NH₂]₂ in 5 mM [Fe(CN)₆]^{3-/4-} containing 0.1 M KCl at different scan rates; (B) The corresponding linear relationship between the redox peak currents and the square root of scan rates for [AC/UiO-66-NH₂]₂.

at GCE modified with different layers of [AC/UiO-66-NH₂]₂ were studied. As presented in Fig. 7A, the stripping currents of Pb²⁺ and Hg²⁺ significantly increase as the layer number increases from one-layer to two-layer. This may be attributed to the fact that the more electrodeposition layers, the more active electrode materials on GCE. However, further increment of the layers number results in a decreased stripping current, which could be related to the obstruction of charge transfer caused by the excessive thick assembly layer. As a result, GCE modified two layers of [AC/UiO-66-NH₂]₂ is selected as the optimal sensing electrode.

The effect of pH on current response was studied from pH 3.0 to 6.0. As shown in Fig. 7B, the peak currents for both ions gradually increase with pH changing from 3.0 to 4.5. This phenomenon is associated with the fact that at low pH, the protonation of amino groups (-NH₃⁺) weakens the adsorption of heavy metal ions. As the pH increases, the protonation degree of amino groups decreases, accompanying with the enhancement of the chelating ability with Pb²⁺ and Hg²⁺. However, when pH is higher than 4.5, the peak currents of Pb²⁺ and Hg²⁺ decrease, resulting from the hydrolysis of Pb²⁺ and Hg²⁺. The maximum DPASV responses are observed at pH 4.5, which is chosen for further experiments.

The influence of deposition time on the stripping currents was examined with deposition time ranging from 90 s to 300 s. As demonstrated in Fig. 7C, the current responses of Pb²⁺ and Hg²⁺ grow linearly

from 90 to 210 s. With the prolonging of deposition time, an increase in the amount Pb²⁺ and Hg²⁺ deposited on the [AC/UiO-66-NH₂]₂/GCE surface. However, when the deposition time exceeds 210 s, the stripping currents basically remain unchanged, which is owing to the saturation of active sites on the electrode surface. Therefore, 210 s is preferentially utilized for further experiments.

The result of deposition potential optimization is shown in Fig. 7D, where the stripping currents of Pb²⁺ and Hg²⁺ increase significantly as the deposition potential changes from -0.4 V to -0.7 V, indicating that the negative shift of the deposition potential promotes the reduction of Pb²⁺ and Hg²⁺ on the surface of [AC/UiO-66-NH₂]₂/GCE. However, with the deposition potential shifts from -0.7 V to -1.0 V, the peak currents remain basically stable. Thus, -0.7 V is select as the optimal deposition potential.

3.4. DPASV detection of Pb²⁺ and Hg²⁺

Under the optimized experimental conditions, the DPASV is applied for the individual determination of Pb²⁺ and Hg²⁺ at [AC/UiO-66-NH₂]₂/GCE. As shown in Fig. 8D, in the presence of 100 µg·L⁻¹ of Hg²⁺, the stripping current of Pb²⁺ shows an increasing tendency with increasing the concentrations of Pb²⁺. A good linear relationship (Fig. 8G) between currents (I) and the square root of Pb²⁺ concentration (C^{1/2}) was displayed in a wide range of 0.001 µg·L⁻¹ to 1000 µg·L⁻¹. The

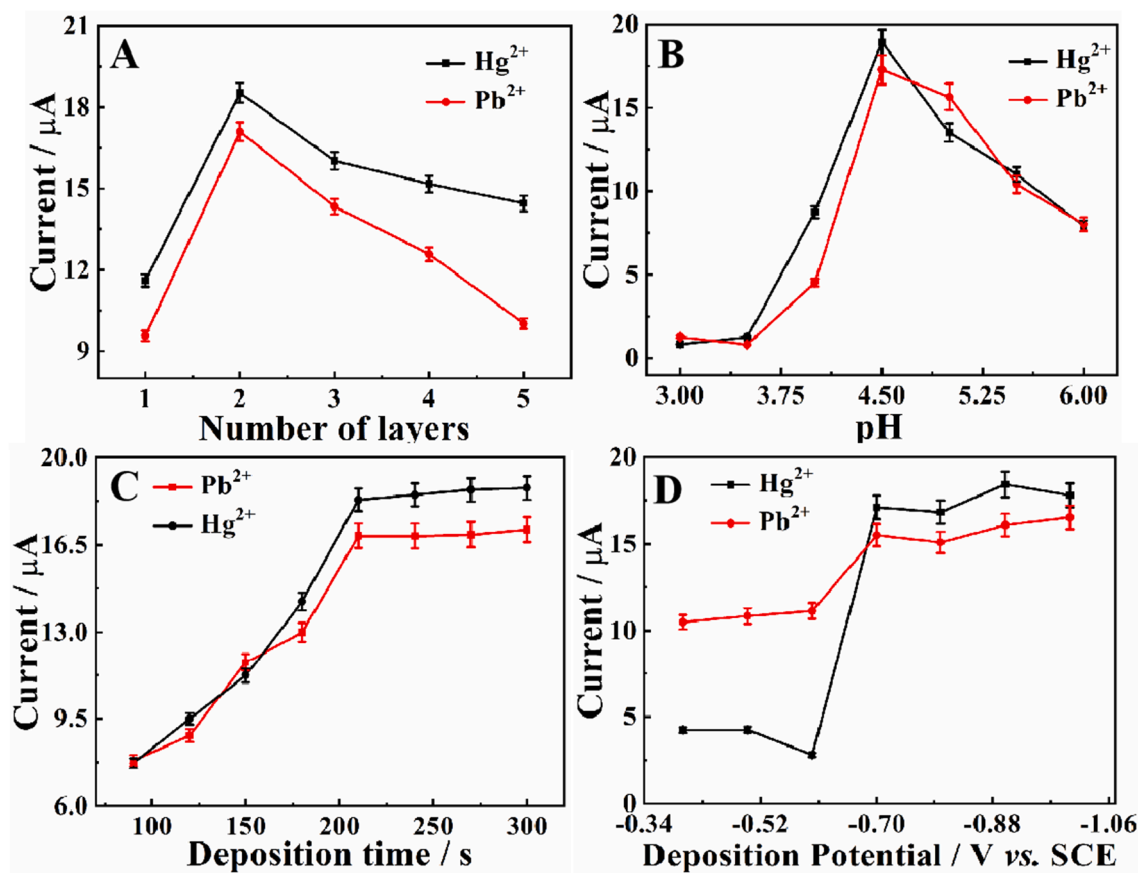


Fig. 7. Optimization of experimental conditions. Influence of (A) number of [AC/UiO-66-NH₂]_n layer, (B) pH value of the detection solution, (C) deposition time, (D) deposition potential on the stripping peak current of Pb²⁺ and Hg²⁺ on the [AC/UiO-66-NH₂]_n/GCE.

calibration equations of $I - C^{1/2}$ is $I (\mu A) = 0.4404 + 1.5293 c^{1/2} (\mu g \cdot L^{-1})$ ($R^2 = 0.9948$). The limit of detection (LOD) was calculated to be $0.3 \text{ ng} \cdot L^{-1}$ for Pb²⁺ at a signal-to-noise ratio (S/N) of 3. Similarly, Fig. 8B shows the response of DPASV to different concentrations of Hg²⁺ in the presence of constant concentration of Pb²⁺ ($100 \mu g \cdot L^{-1}$). As shown, the increment of Hg²⁺ concentration does enhance the peak current of Hg²⁺. The linear regression equation is $I (\mu A) = 0.7697 + 2.5188 c^{1/2} (\mu g \cdot L^{-1})$ ($R^2 = 0.9981$) with the LOD of $0.3 \text{ ng} \cdot L^{-1}$.

The typical signal of DPASV investigation for the simultaneous detection of Pb²⁺ and Hg²⁺ by varying the concentrations of both ions is depicted in Fig. 8C. As shown, two distinct and well-defined peaks appear at -0.56 V and 0.12 V , corresponding to Pb²⁺ and Hg²⁺, respectively. Both the peak currents enhance with the increment of concentration of Pb²⁺ and Hg²⁺ from $0.003 \mu g \cdot L^{-1}$ to $1000 \mu g \cdot L^{-1}$ (Fig. 8F). The linear regression equations of Pb²⁺ and Hg²⁺ could be obtained as $I (\mu A) = 0.5771 + 1.642 c^{1/2} (\mu g \cdot L^{-1})$ ($R^2 = 0.9959$) and $I (\mu A) = 0.1676 + 1.7904 c^{1/2} (\mu g \cdot L^{-1})$ ($R^2 = 0.9995$) (Fig. 8D), respectively. Both the LODs of Pb²⁺ and Hg²⁺ could be calculated as $1 \text{ ng} \cdot L^{-1}$, which are far lower than the allowable values ($10 \mu g \cdot L^{-1}$ Pb²⁺ and $6 \mu g \cdot L^{-1}$ for Hg²⁺ [40] of drinking water) stipulated by the World Health Organization (WHO). The sensing characteristics of the proposed [AC/UiO-66-NH₂]₂ and other reported electrochemical Pb²⁺ and Hg²⁺ sensors are summarized in Table 2. By comparison, the [AC/UiO-66-NH₂]₂/GCE displays wider linear range and lower LOD for Pb²⁺ and Hg²⁺. These attractive features are attributed to the synergistic effect between AC and UiO-66-NH₂.

3.5. Intelligent analysis of Pb²⁺ and Hg²⁺ via modeling

In this work, the relationships between the stripping currents for

Pb²⁺ and Hg²⁺ and their concentrations were non-linear with traditional regression analysis (Fig. 8D, Fig. 8E and Fig. 8F). After the transform of analytes concentrations into their square root (Fig. 8G, Fig. 8H and Fig. 8I), a linear regression model was obtained. However, this processing reinforces the concept of nonlinearity and leads to over-fitting or under-fitting, or even to an inability to fully reflect the true features of initial data. In order to deal well with this nonlinear problem, ANNs were employed to build the multivariate calibration models. Fig. 8J-L show the ANN models for quantitative determination of Pb²⁺ and Hg²⁺. From the model prediction curve, the proposed ANN model can well forecast the values of Pb²⁺ and Hg²⁺ concentration, even if the slope of the graph shifts.

In ANN model, the number of inputs was equivalent to the number of independent variables, that is the concentration of Pb²⁺ and Hg²⁺. The number of neurons in the output layer equals to the number of output variables of the model, that is, the current corresponding to the voltammetric response. Fig. 9 plots the predicted ANN values against the actual concentrations of Pb²⁺ and Hg²⁺ samples tested simultaneously for comparison and calculates the comparison regression line. Coefficient of determination (R^2) close to 1 indicates the desirable efficiency of the ANN method. MAD is 0.4674 and 0.6739, RMSE is 7.0375 and 5.3086, respectively and they are in a very small range and acceptable. The results show that the model is well fitted and has good prediction ability in the analysis of Pb²⁺ and Hg²⁺. From Table 3, it can be observed that R_C^2 is between 0.9964 and 0.9997, $RMSE_C$ is between 0.4948 and 1.8826, and MAE is between 0.5452 and 1.1384. R_{CV}^2 and $RMSE_{CV}$ range from 0.9624 to 0.9823 and 2.1182 to 2.9348, respectively.

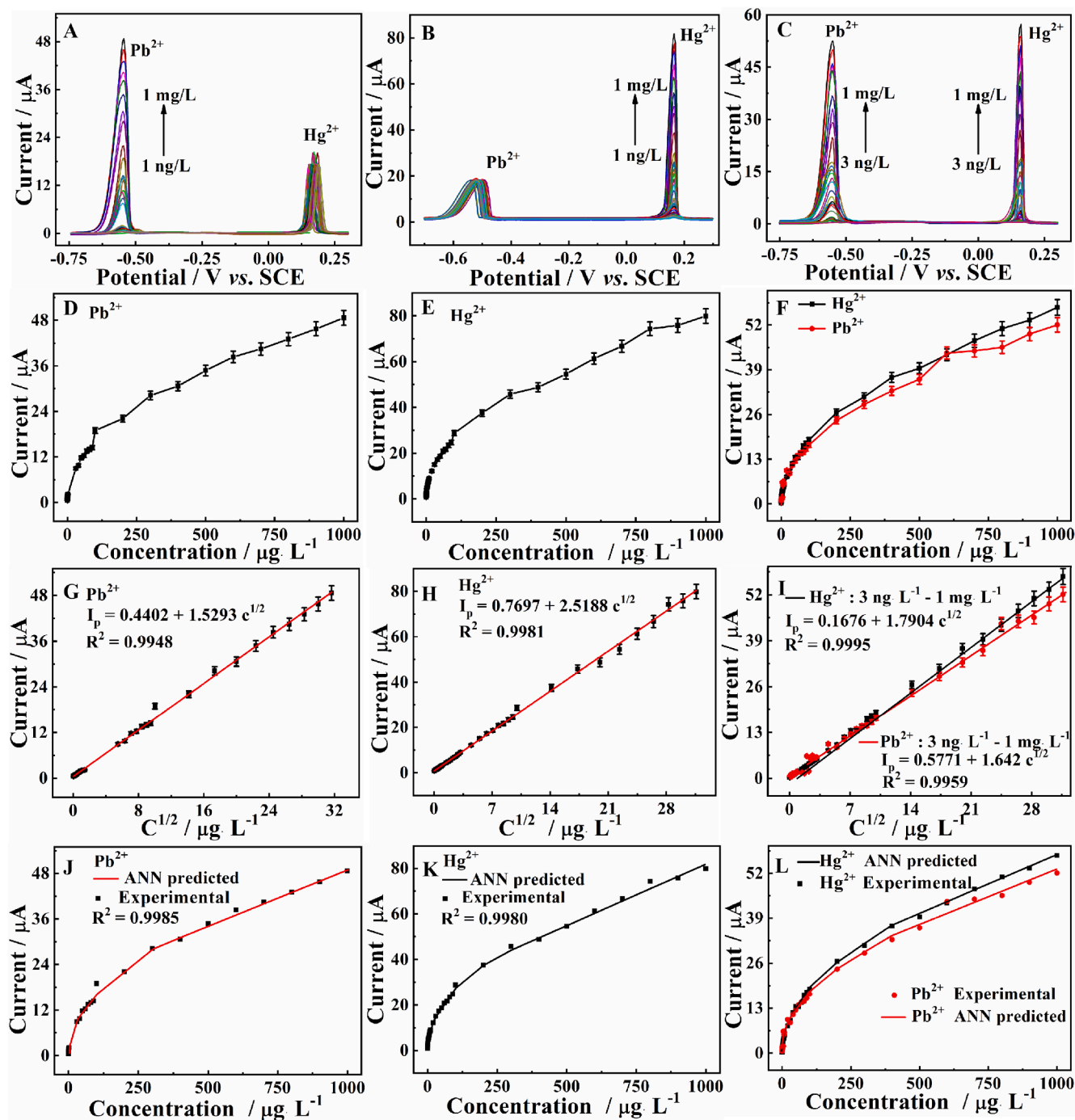


Fig. 8. A simultaneous analysis of Pb²⁺ and Hg²⁺ (A-C); The corresponding relationship curves of (D) Pb²⁺, (E) Hg²⁺ and (F) Pb²⁺ and Hg²⁺ between I and C; The corresponding calibration curves (G, H, I) between I and C^{1/2}, and (J, K, L) the fitting analysis of ANN method.

3.6. Repeatability, reproducibility, stability, and selectivity of [AC/UiO-66-NH₂]₂/GCE

To evaluate the repeatability of the designed electrochemical sensor, the sensing performance of [AC/UiO-66-NH₂]₂/GCE was investigated for 15 consecutive measurements (Fig. 10A). The RSDs of Pb²⁺ and Hg²⁺ are 2.78% and 2.65%, respectively, showing the sensor owns satisfactory repeatability. Five parallel electrodes were prepared to estimate the reproducibility of [AC/UiO-66-NH₂]₂/GCE under the same conditions. The RSDs are 2.64% of Pb²⁺ and 3.18% of Hg²⁺ (Fig. 10B), indicating [AC/UiO-66-NH₂]₂/GCE has good reproducibility.

In addition, the long-term stability of [AC/UiO-66-NH₂]₂/GCE was

studied by monitoring 100 μg·L⁻¹ Pb²⁺ and 100 μg·L⁻¹ Hg²⁺ daily after stored at room temperature for 15 days. As shown in Fig. 10C, the DPASV response for Pb²⁺ and Hg²⁺ retain 91.05% and 92.83% of the initial values after 15 days of storage, suggesting an acceptable stability of [AC/UiO-66-NH₂]₂/GCE.

The selectivity for 100 μg·L⁻¹ Pb²⁺ and 100 μg·L⁻¹ Hg²⁺ was evaluated in the mixed solution containing interfering metal ions including 50-fold K⁺, Na⁺, SO₄²⁻, Zn²⁺, Al³⁺, NO₃⁻, Co²⁺, Ni²⁺, Cl⁻, Mn²⁺, Cd²⁺, Cu²⁺. As presented in Fig. 10D, the current responses of Pb²⁺ and Hg²⁺ fluctuates within 10% in the presence various interfering ions. The result indicates the prepared electrode has strong selectivity for Pb²⁺ and Hg²⁺, which might be ascribed to the fact that abundant channels in

Table 2Comparison of analytical performance of various reported electrochemical sensors for measurement of Pb^{2+} and Hg^{2+} .

Electrode Substrate	Measurement Technique	Linear range ($\mu\text{g}\cdot\text{L}^{-1}$)	LOD ($\mu\text{g}\cdot\text{L}^{-1}$)		Reference
			Pb^{2+}	Hg^{2+}	
Zr-DMBD MOFs ^a /3D-KSC ^b /GCE	SWASV	50.15–702.1	–	10.03	[41]
trGNO ^c /Fc ^d -NH ₂ -UiO-66/GCE	DPASV	0.2072–414.4	0.124	–	[42]
Ru@UiO-66-NH ₂ /GCE	fluorescence	20.06–10030	–	10.63	[43]
Pd@PAC ^e /GCE	SWASV	5.18–103.6	1.368	–	[44]
rGO/SMOF ^f /PEI ^g /SPCE ^h	DPV	103.6–2693.6, 200.6–1003	25.07	107.7	[45]
pg-C ₃ N ₄ ⁱ /CoMn ₂ O ₄ /GCE	SWASV	41.44–911.68	2.901	–	[46]
N,S-doped C@Pd nanorods/GCE	DPSV	0.108–1003	–	0.036	[47]
[AC/UiO-66-NH ₂] ₂ /GCE	DPASV	0.003–1000	0.001	0.001	This work

Note: a:Zr-DMBD MOFs, 2,5-dimercaptoterephthalic acid; b:3D-KSC, three-dimensional macroporous carbon; c:trGNO, thermally reduced graphene oxide; d:Fc, ferrocenecarboxylic; e:PAC, porous activated carbon; f:SMOF, single walled carbon nanotubes and MOF; g:PEI, polyethyleneimine; h:SPCE, screen-printed carbon electrode; i:pg-C₃N₄, porous graphitic carbon nitride.

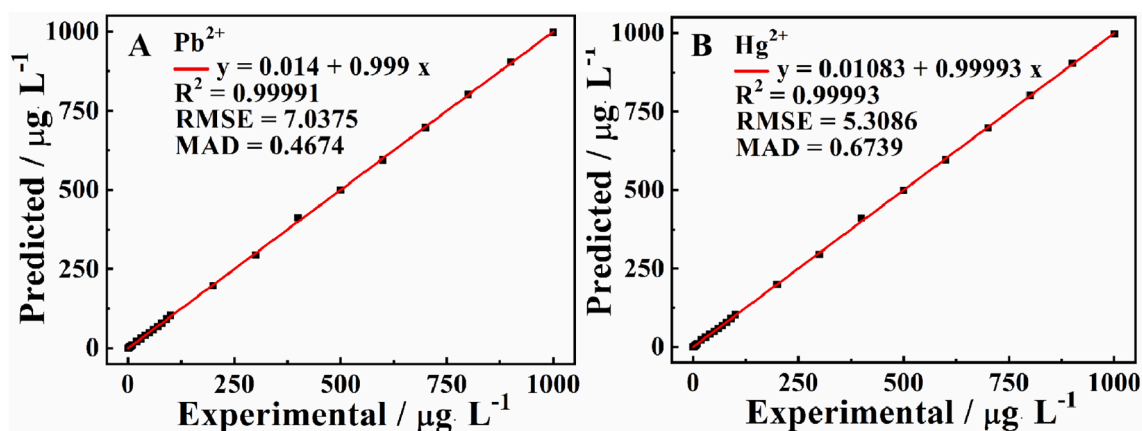


Fig. 9. Comparison of the concentration experimental and ANN predicted values of (A) Pb^{2+} , (B) Hg^{2+} during the simultaneous detection of Pb^{2+} and Hg^{2+} .

Table 3Recoveries and RSD obtained from practical samples spiked with Pb^{2+} and Hg^{2+} using ANN and ASS method ($n = 3$).

model	calibration set			cross validation set	
	R_c^2	RMSE _C	MAE	R_{cv}^2	RMSE _{CV}
Hg^{2+} in 100 $\mu\text{g}\cdot\text{L}^{-1}$ Pb^{2+}	0.9964	1.8826	1.1384	0.9624	2.9348
Pb^{2+} in 100 $\mu\text{g}\cdot\text{L}^{-1}$ Hg^{2+}	0.9997	0.4948	0.5452	0.9692	2.5635
Hg^{2+} (simultaneous detection)	0.9967	0.9947	0.8920	0.9823	2.3079
Pb^{2+} (simultaneous detection)	0.9966	0.8505	0.8132	0.9819	2.1182

[AC/UiO-66-NH₂]₂ permit the size and shape-selectivity over the guests [48]. In addition, Pb^{2+} and Hg^{2+} can form strong chelation with the -N groups [19]. All of these enable the material to be applied for simultaneous determination of Pb^{2+} and Hg^{2+} in real samples.

3.7. Performance evaluation of ANN for practical application

To verify the applicability of [AC/UiO-66-NH₂]₂/GCE, the contents of Pb^{2+} and Hg^{2+} were detected in lake water and paddy water by standard addition method. Both the samples were collected from Jiangxi Agricultural University. The water samples were filtered through a 0.22 μm filter and then diluted to 100 folds with 0.1 M acetate buffer solution (pH 4.5). A standard solution of Pb^{2+} and Hg^{2+} with various concentrations (0, 0.5, 5.0 and 10.0 $\mu\text{g}\cdot\text{L}^{-1}$) was spiked separately into the water samples, and tested using [AC/UiO-66-NH₂]₂/GCE. As shown in Table 4, the results of ANN analysis reveal that the spiked recoveries of Pb^{2+} and Hg^{2+} in paddy water are 96.60%–101.4% and 95.93–100.3%, respectively. As for the lake water, the recoveries of

Pb^{2+} and Hg^{2+} are 98.00%–101.3% and 97.67–100.5%, respectively. All the RSDs are less than 5% ($n = 3$). In addition, the ANN results are verified by atomic absorption spectrometry (AAS) and the observed results from both tactics are in good agreement. These results indicate the feasible and reliable of [AC/UiO-66-NH₂]₂/GCE for the intelligent detection of Pb^{2+} and Hg^{2+} in real samples.

4. Conclusions

In this work, [AC/UiO-66-NH₂]₂ modified GCE through LbL assembling has been successfully obtained for simultaneous detection of Pb^{2+} and Hg^{2+} in water samples. On account of the large specific surface area, plentiful active sites, and high conductivity, [AC/UiO-66-NH₂]₂ is helpful to the enrichment and transportation of electrolytes and promotes the electron transfer. Accordingly, the proposed sensor presents wide linear ranges with low detection limits of 1.0 $\text{ng}\cdot\text{L}^{-1}$ for both Pb^{2+} and Hg^{2+} . Besides, the [AC/UiO-66-NH₂]₂/GCE provides good repeatability, reproducibility, and good selectivity. Finally, the integration of [AC/UiO-66-NH₂]₂/GCE and ANN algorithm was proved to be effective sensing platform for intelligent analysis of Hg^{2+} and Pb^{2+} in river water and paddy water.

CRedit authorship contribution statement

Jin Zou: Conceptualization, Methodology, Writing – original draft, Funding acquisition. **Wenbin Qian:** Methodology, Investigation, Validation. **Yihui Li:** Methodology, Formal analysis, Writing – review & editing. **Qi Yu:** Methodology, Writing – review & editing. **Yongfang Yu:** Investigation, Validation. **Shangxing Chen:** Supervision, Project administration, Funding acquisition, Writing – review & editing. **Fengli**

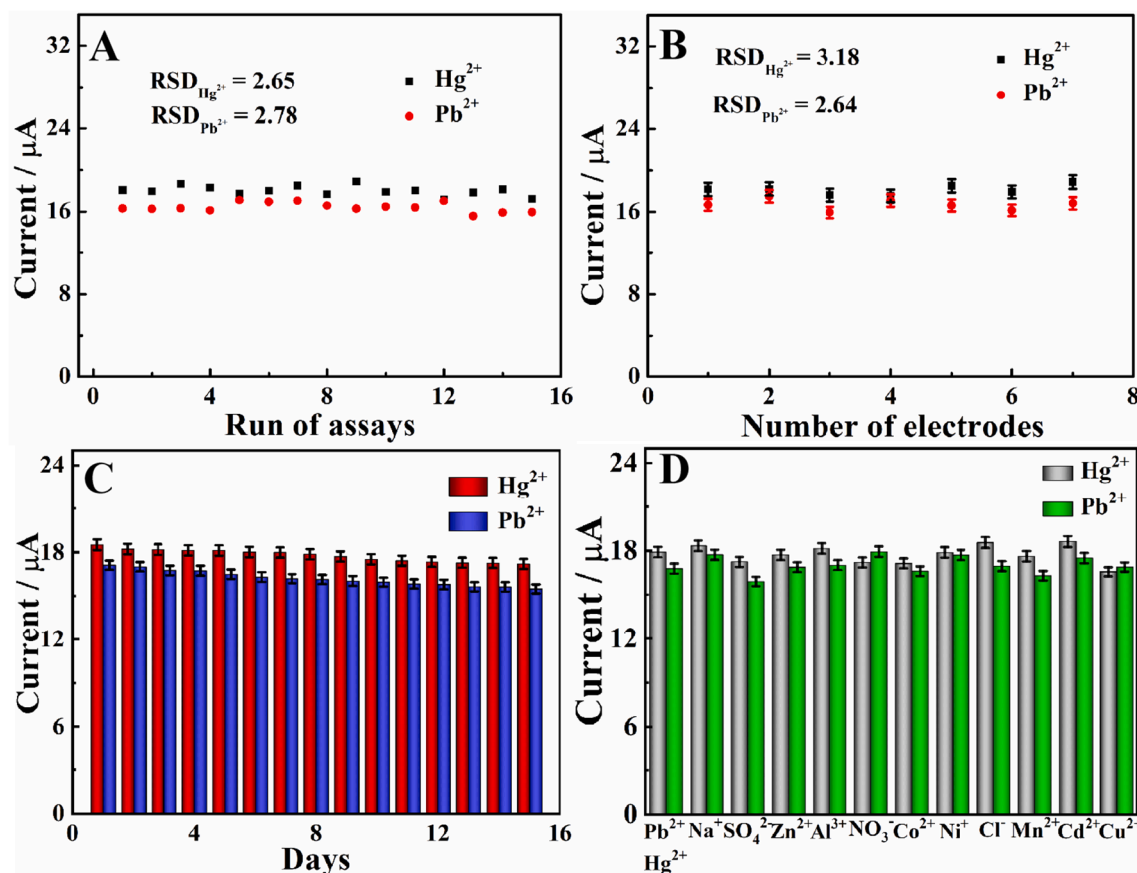


Fig. 10. (A) Repeatability measurements for one [AC/Uio-66-NH₂]₂/GCE; (B) Reproducibility measurements at seven independent [AC/Uio-66-NH₂]₂/GCEs; (C) Stability measurements at [AC/Uio-66-NH₂]₂/GCE within 15 days; (D) Selectivity of [AC/Uio-66-NH₂]₂/GCE.

Table 4

Recoveries and RSD obtained from practical samples spiked with Pb²⁺ and Hg²⁺ using ANN and AAS method (n = 3).

Sample	Analyte	Added (µg/L)	ANN method Found (µg/L)	RSD (%)	Recovery (%)	AAS method Found (µg/L)	RSD (%)	Recovery (%)	
Paddy water	Pb ²⁺	0	–	–	–	–	–	–	
		0.5	0.48 ± 0.01	1.69	96.60	0.51 ± 0.02	3.92	102.0	
		5.0	5.07 ± 0.10	2.00	101.4	5.12 ± 0.25	4.82	102.5	
	Hg ²⁺	10	9.81 ± 0.18	1.80	98.07	9.99 ± 0.35	3.47	99.93	
		0	–	–	–	–	–	–	–
		0.5	0.49 ± 0.03	3.09	98.67	0.53 ± 0.01	2.70	106.8	
Lake water	Pb ²⁺	5.0	5.02 ± 0.16	3.20	100.3	4.89 ± 0.23	4.62	97.80	
		10	9.59 ± 0.12	1.29	95.93	10.01 ± 0.34	3.38	100.1	
		0	–	–	–	–	–	–	–
	Hg ²⁺	0.5	0.49 ± 0.02	4.13	97.67	0.48 ± 0.02	3.16	96.67	
		5.0	4.91 ± 0.21	4.23	98.27	5.34 ± 0.15	2.82	106.7	
		10	10.13 ± 0.46	4.52	101.3	9.73 ± 0.17	1.71	97.27	
Hg ²⁺	0	–	–	–	–	–	–	–	
	0.5	0.49 ± 0.02	4.08	98.00	0.51 ± 0.02	3.01	101.3		
	5.0	5.03 ± 0.23	4.67	100.5	5.08 ± 0.17	3.36	101.5		
		10	9.77 ± 0.37	3.80	97.73	9.69 ± 0.41	4.26	96.87	

Qu: Investigation, Visualization. **Yansha Gao:** Writing – review & editing, Investigation, Visualization. **Limin Lu:** Supervision, Project administration, Funding acquisition, Writing – review & editing.

Declaration of Competing Interest

The authors declare that they have no known competing financial interests or personal relationships that could have appeared to influence the work reported in this paper.

Acknowledgements

We are grateful to the National Natural Science Foundation of China (22064010, 51862014, 31960295, 21665010, 31741103, and 51302117), the Academic and technical leader of major disciplines in Jiangxi Province Training Program Leading Talents Project (20204BCJ22022), the Natural Science Foundation of Jiangxi Province (20202ACBL213009, 20192BBEL50029), Jiangxi Outstanding Young Talents Funding Scheme (20162BCB23030), Provincial Projects for Postgraduate Innovation in Jiangxi (YC2019-S182), and Natural Science Foundation of Nanchang City (No. 2018CXTD014) for their financial

support of this work.

References

- X. Guo, S.B. Sang, A.Q. Jian, S. Gao, Q.Q. Duan, J.L. Ji, Q. Zhang, W.D. Zhang, A bovine serum albumin-coated magnetoelastic biosensor for the wireless detection of heavy metal ions, *Sens. Actuators. B Chem.* 256 (2017) 318–324, <https://doi.org/10.1016/j.snb.2017.10.040>.
- P. Li, D.Z. Zhang, C.X. Jiang, X.Q. Zong, Y.H. Cao, Ultra-sensitive suspended atomically thin-layered black phosphorus mercury sensors, *Biosens. Bioelectron.* 98 (2017) 68–75, <https://doi.org/10.1016/j.bios.2017.06.027>.
- P. Li, D.Z. Zhang, Z.L. Wu, Flexible MoS₂ sensor arrays for high performance label-free ion sensing, *Sens. Actuators, A* 286 (2018) 51–58, <https://doi.org/10.1016/j.sna.2018.12.026>.
- P. Li, D.Z. Zhang, J.F. Wu, Y.H. Cao, Z.L. Wu, Flexible integrated black phosphorus sensor arrays for high performance ion sensing, *Sens. Actuators. B Chem.* 273 (2018) 358–364, <https://doi.org/10.1016/j.snb.2018.06.077>.
- W. Zhong, F. Gao, J. Zou, S.W. Liu, M.F. Li, Y.S. Gao, Y.F. Yu, X.Q. Wang, L.M. Lu, MXene@Ag-based ratiometric electrochemical sensing strategy for effective detection of carbendazim in vegetable samples, *Food Chem.* 360 (2021) 130006–130012, <https://doi.org/10.1016/j.foodchem.2021.130006>.
- X.L. Qiu, L.M. Lu, J. Leng, Y.F. Yu, W.M. Wang, M. Jiang, L. Bai, An enhanced electrochemical platform based on graphene oxide and multi-walled carbon nanotubes nanocomposite for sensitive determination of Sunset Yellow and Tartrazine, *Food Chem.* 190 (2016) 889–895, <https://doi.org/10.1016/j.foodchem.2015.06.045>.
- X.L. Tu, F. Gao, X. Ma, J. Zou, Y.F. Yu, M.F. Li, F.L. Qu, X.G. Huang, L.M. Lu, Mxene/carbon nanohorn/ β -cyclodextrin-Metal-organic frameworks as high-performance electrochemical sensing platform for sensitive detection of carbendazim pesticide, *J. Hazard. Mater.* 396 (2020) 122776–122784, <https://doi.org/10.1016/j.jhazmat.2020.122776>.
- M. Qiu, C.J. He, Efficient removal of heavy metal ions by forward osmosis membrane with a polydopamine modified zeolitic imidazolate framework incorporated selective layer, *J. Hazard. Mater.* 367 (2018) 339–347, <https://doi.org/10.1016/j.jhazmat.2018.12.096>.
- L. Ma, X. Zhang, M. Ikrama, M. Ullaha, H. Wu, K. Shi, Controllable synthesis of an intercalated ZIF-67/EG structure for the detection of ultratrace Cd²⁺, Cu²⁺, Hg²⁺ and Pb²⁺ ions, *Chem. Eng. J.* 395 (2020) 125216–125227, <https://doi.org/10.1016/j.cej.2020.125216>.
- S. Singh, A. Numan, Y. Zhan, V. Singh, T.V. Hung, N.D. Nam, A novel highly efficient and ultrasensitive electrochemical detection of toxic mercury (II) ions in canned tuna fish and tap water based on a copper metal-organic framework, *J. Hazard. Mater.* 399 (2020) 123042–123050, <https://doi.org/10.1016/j.jhazmat.2020.123042>.
- A. Radwan, I.M. El-Sewify, A. Shahat, H.M.E. Azzazy, M.M.H. Khalil, M.F. El-Shahat, Multiuse Al-MOF Chemosensors for Visual Detection and Removal of Mercury Ions in Water and Skin-Whitening Cosmetics, *ACS Sustainable Chem. Eng.* 8 (2020) 15097–15107, <https://doi.org/10.1021/acssuschemeng.0c03592>.
- Y.W. Zhao, Y.J. Zhang, A.R. Liu, Z.Z. Wei, S.Q. Liu, Construction of Three-Dimensional Hemin-Functionalized Graphene Hydrogel with High Mechanical Stability and Adsorption Capacity for Enhancing Photodegradation of Methylene Blue, *ACS Appl. Mater. Interfaces* 9 (2017) 4006–4014, <https://doi.org/10.1021/acsaami.6b10959>.
- S. Kurbanoglu, L. Rivas, S.A. Ozkan, A. Merkoçi, Electrochemically reduced graphene and iridium oxide nanoparticles for inhibition-based angiotensin-converting enzyme inhibitor detection, *Biosens. Bioelectron.* 88 (2016) 122–129, <https://doi.org/10.1016/j.bios.2016.07.109>.
- X. Hui, M. Sharifuzzaman, S. Sharma, X. Xuan, S.P. Zhang, S.G. Ko, S.H. Yoon, J. Y. Park, High-Performance Flexible Electrochemical Heavy Metal Sensor Based on Layer-by-Layer Assembly of Ti₃C₂Tx/MWNTs Nanocomposites for Noninvasive Detection of Copper and Zinc Ions in Human Biofluids, *ACS Appl. Mater. Interfaces* 12 (2020) 48928–48937, <https://doi.org/10.1021/acsaami.0c12239>.
- J. Jaramillo, V. Gómez-Serrano, P.M. Álvarez, Enhanced adsorption of metal ions onto functionalized granular activated carbons prepared from cherry stones, *J. Hazard. Mater.* 161 (2008) 670–676, <https://doi.org/10.1016/j.jhazmat.2008.04.009>.
- Y. Fan, B. Wang, S.H. Yuan, X.H. Wu, J. Chen, L.L. Wang, Adsorptive removal of chloramphenicol from wastewater by NaOH modified bamboo charcoal, *Bioresour. Technol.* 101 (2010) 7661–7664, <https://doi.org/10.1016/j.biortech.2010.04.046>.
- J.J. Richardson, M. Bjornmalm, F. Caruso, Technology-driven layer-by-layer assembly of nanofilms, *Sci.* 348 (2015) 2491–2502, <https://doi.org/10.1126/science.aaa2491>.
- Z. Lu, W. Zhao, L. Wu, J. He, W. Dai, C. Zhou, H. Du, J. Ye, Tunable electrochemical of electro-synthesized layer-by-layer multilayer films based on multi-walled carbon nanotubes and metal-organic framework as high-performance electrochemical sensor for simultaneous determination cadmium and lead, *Sens. Actuators. B Chem.* 326 (2020) 128957–128965, <https://doi.org/10.1016/j.snb.2020.128957>.
- L.D. Ji, J. Wang, K.B. Wu, N.J. Yang, Tunable Electrochemistry of Electro-synthesized Copper Metal-Organic Frameworks, *Adv. Funct. Mater.* 28 (2017) 1706961.1–1706961.8, <https://doi.org/10.1002/adfm.201706961>.
- G. Valdés-Ramírez, M. Gutiérrez, M.D. Valle, M. Ramírez-Silva, D. Fournier, J. Marty, Automated resolution of dichlorvos and methylparaoxon pesticide mixtures employing a Flow Injection system with an inhibition electronic tongue, *Biosens. Bioelectron.* 24 (2008) 1103–1108, <https://doi.org/10.1016/j.bios.2008.06.022>.
- Y.Y. Sheng, W.B. Qian, J.P. Huang, B.L. Wu, J. Yang, T. Xue, Y. Ge, Y.P. Wen, Electrochemical detection combined with machine learning for intelligent sensing of maleic hydrazide by using carboxylated PEDOT modified with copper nanoparticles, *Microchim. Acta.* 186 (2019) 543–554, <https://doi.org/10.1007/s00604-019-3652-x>.
- N. Maleki, S. Kashanian, E. Maleki, M. Nazari, A novel enzyme-based biosensor for catechol detection in water samples using artificial neural network, *Biochem. Eng. J.* 128 (2017) 1–11, <https://doi.org/10.1016/j.bej.2017.09.005>.
- K.P. Ferentinos, C.P. Yialouris, P. Blouchos, G. Moschopoulou, V. Tsourou, S. Kintzios, The use of artificial neural networks as a component of a cell-based biosensor device for the detection of pesticides, *Procedia Eng.* 47 (2012) 989–992, <https://doi.org/10.1016/j.proeng.2012.09.313>.
- X.Y. Zhu, L. Lin, R.M. Wu, Y.F. Zhu, Y.Y. Sheng, P.C. Nie, P. Liu, L.L. Xu, Y.P. Wen, Portable wireless intelligent sensing of ultra-trace phytoestrogen α -naphthalene acetic acid using self-assembled phosphorene/Ti₃C₂-MXene nanohybrid with high ambient stability on laser induced porous graphene as nanzyme flexible electrode, *Biosens. Bioelectron.* 179 (2021) 113062–113070, <https://doi.org/10.1016/j.bios.2021.113062>.
- Y. Wang, L. Wang, W. Huang, T. Zhang, X.Y. Hu, J.A. Perman, S.Q. Ma, A metal-organic framework and conducting polymer based electrochemical sensor for high performance cadmium ion detection, *J. Mater. Chem. A* 5 (2017) 8385–8393, <https://doi.org/10.1039/C7TA01066D>.
- H. Hu, F. Yan, S.K. Wang, L.L. Si, B.F. Li, Immunomodulatory activity of Alaska pollock hydrolysates obtained by glutamic acid biosensor-artificial neural network and the identification of its active central fragment, *J. Funct. Foods* 24 (2016) 37–47, <https://doi.org/10.1016/j.jff.2016.03.033>.
- D.Z. Zhang, J.J. Liu, C.X. Jiang, A.M. Liu, B.K. Xia, Quantitative detection of formaldehyde and ammonia gas via metal oxide-modified graphene-based sensor array combining with neural network model, *Sens. Actuators. B Chem.* 240 (2017) 55–65, <https://doi.org/10.1016/j.snb.2016.08.085>.
- S. Mofavvaz, M.R. Sohrabi, A. Nezamzadeh-Ejhi, New model for prediction binary mixture of antihistamine decongestant using artificial neural networks and least squares support vector machine by spectrophotometry method, *Spectrochim. Acta A Mol. Biomol. Spectrosc.* 182 (2017) 105–115, <https://doi.org/10.1016/j.saa.2017.04.001>.
- Y.L. Wang, H.Q. Xuan, G.X. Lin, F. Wang, Z. Chen, X.P. Dong, A melamine-assisted chemical blowing synthesis of N-doped activated carbon sheets for super capacitor application, *J. Power Sources.* 319 (2016) 262–270, <https://doi.org/10.1016/j.jpowsour.2016.04.069>.
- G. Singh, I.Y. Kim, K.S. Lakhi, P. Srivastava, R. Naidu, A. Vinu, Single step synthesis of activated bio-carbons with a high surface area and their excellent CO₂ adsorption capacity, *Carbon* 116 (2017) 448–455, <https://doi.org/10.1016/j.carbon.2017.02.015>.
- J. Xu, S. He, H.L. Zhang, J.C. Huang, H.X. Lin, X.X. Wang, J.L. Long, Layered metal-organic framework/graphene nanoarchitectures for organic photosynthesis under visible light, *J. Mater. Chem. A* 3 (2015) 24261–24271, <https://doi.org/10.1039/C5TA06838J>.
- H. Yu, C. Liu, Y. Li, A. Huang, Functionalized Metal-Organic Framework UiO-66-NH-BQB for selective detection of hydrogen sulfide and cysteine, *ACS Appl. Mater. Interfaces* 11 (2019) 41972–41978, <https://doi.org/10.1021/acsaami.9b16529>.
- Z.S. Wu, Y. Sun, Y.Z. Tan, S.B. Yang, X.L. Feng, K. Mullen, Three-Dimensional Graphene-Based Macro- and Mesoporous Frameworks for High-Performance Electrochemical Capacitive Energy Storage, *J. Am. Chem. Soc.* 134 (2012) 19532–19535, <https://doi.org/10.1021/ja308676h>.
- W. Xu, Z. Qin, Y.T. Hao, Q. He, S. Chen, Z.S. Zhang, D. Peng, H.Y. Wen, J. Chen, J. F. Qiu, C.R. Li, A signal-decreased electrochemical immunosensor for the sensitive detection of LAG-3 protein based on a hollow nanobox-MOFs/AuPt alloy, *Biosens. Bioelectron.* 113 (2018) 148–156, <https://doi.org/10.1016/j.bios.2018.05.010>.
- H.L. Shi, F.D. Zhu, X. Zhou, H. Li, F.C. Yang, X. Zhang, J.T. Liu, Large scale fabrication of disposable carbon cloth electrochemical sensors for simultaneous determination of heavy metal ion, *J. Electroanal. Chem.* 840 (2019) 328–337, <https://doi.org/10.1016/j.jelechem.2019.04.001>.
- K.S. Shi, Y. Xie, Y.P. Qiu, Natural oxidation of a temperature series of biochars: opposite effect on the sorption of aromatic cationic herbicides, *Ecoxicol. Environ. Saf.* 114 (2015) 102–108, <https://doi.org/10.1016/j.ecoenv.2015.01.015>.
- D. Zhu, Q.F. Zhen, J.J. Xin, H.Y. Ma, L.C. Tan, H.J. Pang, X.M. Wang, A free-standing and flexible phosphorus/nitrogen dual-doped three-dimensional reticular porous carbon frameworks encapsulated cobalt phosphide with superior performance for nitrite detection in drinking water and sausage samples, *Sens. Actuators. B Chem.* 321 (2020) 128541–128552, <https://doi.org/10.1016/j.snb.2020.128541>.
- D. Zhu, M.Y. Chu, J.J. Xin, X.M. Wang, K.P.O. Halloran, H.Y. Ma, H.J. Pang, L. C. Tan, G.X. Yang, Hierarchical and hollow boron/nitrogen co-doped yolk-shell mesoporous carbon nanospheres attached to reduced graphene oxide with high sensing performance for the simultaneous detection of xanthine and guanosine, *Sens. Actuators. B Chem.* 343 (2021) 130068–130082, <https://doi.org/10.1016/j.snb.2021.130068>.
- M.B. Gumpu, S. Sethuraman, U.M. Krishnan, J.B.B. Rayappan, A review on detection of heavy metal ions in water-An electrochemical approach, *Sens. Actuators. B Chem.* 213 (2015) 515–533, <https://doi.org/10.1016/j.snb.2015.02.122>.

- [41] H.L. Yang, C.W. Peng, J.J. Han, Y.H. Song, L. Wang, Three-dimensional macroporous Carbon/Zr-2,5-dimercaptoterephthalic acid metal-organic frameworks nanocomposites for removal and detection of Hg(II), *Sens. Actuators. B Chem.* 320 (2020) 128447–128453, <https://doi.org/10.1016/j.snb.2020.128447>.
- [42] X.X. Wang, Y.X. Qi, Y. Shen, Y. Yuan, L.D. Zhang, C.Y. Zhang, Y.H. Sun, A ratiometric electrochemical sensor for simultaneous detection of multiple heavy metal ions based on ferrocene-functionalized metal-organic framework, *Sens. Actuators. B Chem.* 310 (2020) 127756–127768, <https://doi.org/10.1016/j.snb.2020.127756>.
- [43] P. Jia, K.R. Yang, J.J. Hou, Y.Y. Cao, X. Wang, L. Wang, Ingenious dual-emitting Ru@UiO-66-NH₂ composite as ratiometric fluorescence sensor for detection of mercury in aqueous, *J. Hazard. Mater.* 408 (2020) 124469–124476, [10.1016/j.jhazmat.2020.124469](https://doi.org/10.1016/j.jhazmat.2020.124469).
- [44] T. Zhang, H. Jin, Y. Fang, J.B. Guan, S.J. Ma, Y. Pan, M. Zhang, H. Zhu, X. Liu, M. Du, Detection of trace Cd²⁺, Pb²⁺ and Cu²⁺ ions via porous activated carbon supported palladium nanoparticles modified electrodes using SWASV, *Mater. Chem. Phys.* 225 (2019) 433–442, <https://doi.org/10.1016/j.matchemphys.2019.01.010>.
- [45] Z.Z. Xu, Z.J. Liu, M. Xiao, L.L. Jiang, C.P. Yi, A smartphone-based quantitative point-of-care testing (POCT) system for simultaneous detection of multiple heavy metal ions, *Chem. Eng. J.* 394 (2020) 124966–124974, <https://doi.org/10.1016/j.cej.2020.124966>.
- [46] Y. Wang, Z.G. Nie, X.Y. Li, Y. Zhao, H. Wang, Highly Sensitive and Selective Electrochemical Sensor Based on Porous Graphitic Carbon Nitride/CoMn₂O₄ Nanocomposite toward Heavy Metal Ions, *Sens. Actuators. B Chem.* 346 (2021) 130539–130547, <https://doi.org/10.1016/j.snb.2021.130539>.
- [47] L.Y. Wang, Y.X. Yang, H.H. Liang, N. Wu, X. Peng, L. Wang, Y.H. Song, A novel N,S-rich COF and its derived hollow N,S-doped carbon@Pd nanorods for electrochemical detection of Hg²⁺ and paracetamol, *J. Hazard. Mater.* 409 (2020) 124528–124536, <https://doi.org/10.1016/j.jhazmat.2020.124528>.
- [48] X. Sun, N. Wang, Y. Xie, H.C. Chu, Y. Wang, Y. Wang, In-situ anchoring bimetallic nanoparticles on covalent organic framework as an ultrasensitive electrochemical sensor for levodopa detection, *Talanta* 225 (2020) 122072–122080, <https://doi.org/10.1016/j.talanta.2020.122072>.